SLAC-PUB-1211
(T-E)
March 1973

MEASUREMENT OF ρ^0 AND ϕ MESON ELECTROPRODUCTION*

J. T. Dakin, G. J. Feldman, W. L. Lakin,**
F. Martin, M. L. Perl, E. W. Petraske,† W. T. Toner††

Stanford Linear Accelerator Center
Stanford University, Stanford, California 94305

ABSTRACT

We report measurements of ρ^0 and ϕ electroproduction at 19.5 GeV in a wide-aperture spectrometer which detected the scattered electron and the decay products of the vector mesons. Data are presented for the region of virtual photon mass squared, q^2, -.25 to -2.0 $(GeV/c)^2$ and virtual photoproduction center-of-mass energy squared, s, 10 to 30 GeV^2. As $|q^2|$ increases, the rho mass spectrum shape changes and the momentum transfer distribution broadens. The ratio of the rho cross section to the total cross section decreases from 11% at $q^2=0$ to about 6% at $|q^2| = m_\rho^2$. The ratio for the production of longitudinally to transversely polarized ρ^0 mesons is $.45 \begin{smallmatrix}+.15\\-.10\end{smallmatrix}$ at $|q^2| = m_\rho^2$, and the interference between longitudinal and transverse amplitudes is almost maximal. The relative ϕ meson cross section also decreases as $|q^2|$ increases. Unitary lower bounds on longitudinal-transverse ratio in inelastic electron scattering are derived.

---

*Work supported by the U. S. Atomic Energy Commission.
**Present address: Birmingham Radiation Centre, University of Birmingham, P. O. Box 363, Birmingham B15 2TT, England.
†Present address: Vanderbilt University, Nashville, Tennessee 37203.
††Present address: Rutherford High Energy Laboratory, Chilton, Didcot, Berkshire, England.

(Submitted to Phys. Rev. D.)

I. INTRODUCTION

Many photoproduction processes can be understood by assuming that the photon couples directly to vector meson states. By studying vector meson electroproduction we seek to determine how this coupling evolves as the photon becomes space-like and its polarization has longitudinal as well as transverse components.

We report here measurements of ρ^o and ϕ meson electroproduction which combine high virtual photon energies and the ability to study ρ^o production and decay angular correlations. These measurements were made at the Stanford Linear Accelerator Center (SLAC) using a wide-aperture spark chamber spectrometer. This paper is a more complete account of data reported earlier.[1]

The first attempts to measure ρ^o electroproduction used a missing (ρ^o) mass technique in which the scattered electron and recoil proton were detected in coincidence.[2-3] These experiments suffered from a large background which made the extraction of the vector meson signal difficult. Furthermore, the ρ^o polarization could not be measured in such experiments since the decay pions were not detected. A spectrometer experiment at DESY detected the scattered electron and the pions from the ρ^o decay, but at angles such that only transversely polarized ρ^o mesons could be observed.[4] In addition to the experiment reported here, two other experiments have been performed in which the decay pions can be observed over a wide range of angles. One was performed using a streamer chamber at DESY[5] and the other was performed with a hybrid bubble chamber at SLAC.[6] Both experiments were conducted at lower virtual photoproduction center-of-mass energies than the present experiment. No previous experiments have observed ϕ meson electroproduction.

The electroproduction of vector mesons has been studied theoretically in vector meson dominance (VMD) models[7-8] and by several other approaches.[9] In a recent series of papers, Sakurai and Schildknecht have attempted to understand inelastic electron-nucleon scattering in terms of virtual photon couplings to vector meson states.[10] Their work makes a number of testable predictions for vector meson electroproduction including the prediction that the ratio of longitudinal to transverse ρ^0 production be quite small, about .06 at $|q^2| = m_\rho^2$.

For the most part, this paper will deal with ρ^0 production, with ϕ meson production relegated to Section VI. Kinematics and phenomenology will be discussed in Section II. Section III will describe the apparatus and Section IV will describe the data collection and reduction. The results for ρ^0 production will be given in Section V. Section VII will derive lower bounds to the ratio of longitudinal to transverse total virtual photoproduction cross sections using unitarity and the Schwarz inequality.

II. KINEMATICS AND PHENOMENOLOGY

The rho electroproduction reaction

$$ep \rightarrow ep\,\pi^+\pi^- \qquad (1)$$

can be regarded as an inelastic electron scatter ($e \rightarrow e\gamma^*$), followed by the virtual photoproduction of a rho ($\gamma^* p \rightarrow \rho p$), followed by the rho decay ($\rho \rightarrow \pi^+\pi^-$). Quantities describing the electron scatter are q^2, the square of the four-momentum carried by the photon; ϵ, the photon polarization; and s, the square of the total energy in the $\gamma^* p$ collision as measured in the $\gamma^* p$ center-of-mass. The rho production is characterized by t', the four momentum transfer squared to the proton less its smallest possible value (t_{min}), and ϕ_e, the azimuthal angle between the electron scatter plane and the ρ production plane. θ^* is the

angle between the γ^* and the ρ in the γ^*p center-of-mass. The final $\pi^+\pi^-$ system is described by $m_{\pi\pi}$, its invariant mass; ϕ, the azimuthal angle between the ρ production plane and the ρ decay plane; and θ, the ρ decay polar angle. The definition of the various angles is shown in Fig. 1. It proved useful in the analysis to define an additional angle $\psi \equiv \phi_e + \phi$. In the limit $\theta^* \to 0$, ψ becomes the azimuthal angle between the electron scatter plane and the ρ decay plane.

The electron scatter variables can be expressed as follows

$$q^2 = -4EE' \sin^2(\theta_e/2) \tag{2}$$

$$s = m^2 + 2m\nu + q^2 \tag{3}$$

$$\epsilon = \left\{1 + 2\left[1 - \frac{\nu^2}{q^2}\right]\tan^2(\theta_e/2)\right\}^{-1} \tag{4}$$

where E and E' are the initial and scattered electron energies in the laboratory system, m is the mass of the target proton, $\nu = E - E'$, and the electron mass is neglected. In our metric $q^2 \leq 0$.

The polarization of the virtual photon can be given as the incoherent sum of two pure states, $\vec{\epsilon}_a$ and $\vec{\epsilon}_b$:

$$\vec{\epsilon}_a = \left\{\left[\frac{1}{2}(1+\epsilon)\right]^{\frac{1}{2}},\ 0,\ -\epsilon_L^{\frac{1}{2}}\right\} \tag{5a}$$

$$\vec{\epsilon}_b = \left\{0,\ \left[\frac{1}{2}(1-\epsilon)\right]^{\frac{1}{2}},\ 0\right\}, \tag{5b}$$

where the polarization vector components are transverse in the electron scatter plane, transverse out of the electron scatter plane, and longitudinal, respectively.[11] The parameter ϵ_L is defined.

$$\epsilon_L = \frac{-q^2}{q_0^2}\,\epsilon \quad . \tag{6}$$

We follow the usual practice of absorbing the frame dependent factor $(-q^2/q_0^2)$ into the production cross section and replacing ϵ_L by ϵ. Equation (5a) shows that longitudinally polarized virtual photons will be coherent with virtual photons polarized in the electron scatter plane, allowing the possibility of observing transverse-longitudinal interference effects.

This experiment measures the ratio of the virtual photoproduction cross section for vector meson production to the total virtual photoproduction cross section directly. To obtain virtual photoproduction cross sections in absolute units, it is necessary to specify a convention for the flux of virtual photons. We use the usual Hand convention to relate the electron scattering cross section, $d\sigma/dq^2 ds$ to the total virtual photoproduction cross section $\sigma_{tot}(q^2, s)$ [12]:

$$\frac{d\sigma}{dq^2 ds} = \Gamma \sigma_{tot}(q^2, s) \tag{7}$$

where

$$\Gamma = \frac{\alpha}{8\pi} \frac{s - m^2}{m^2 E^2 (-q^2)(1-\epsilon)} \quad . \tag{8}$$

III. APPARATUS

The experimental apparatus consisted of a 19.5 GeV electron beam incident on a 4 cm liquid hydrogen target and a large aperture spectrometer to detect a large fraction of the forward final state particles with lab momenta greater than ~ 1 GeV/c. These elements are shown in Fig. 2 and discussed in greater detail below.

The electron beam contained typically 10^4 e^- per 1.5 μsec long SLAC pulse. At the experimental target, the beam had an rms width of 0.5 mm $\times$ 0.5 mm and an rms divergence less than 0.2 mrad $\times$ 0.2 mrad. There the

beam was very well collimated, with fewer than 1 in 10^5 e^- outside a 0.5 cm diameter circle. The momentum spread in the beam was 0.2%.

The spectrometer magnet has 1.37 m diameter pole faces separated by 0.91 m. It was centered on the beam line, 2.54 m downstream from the target, with its principal field component horizontal. At the magnet center, this field was 10 kG and the field integral 17 kG-meters.

The unscattered beam and the forward electromagnetic backgrounds passed through the magnet in a field-free region created by a cylindrical superconducting tube.[13] Beyond the magnet were two optical spark chambers separated by 1.7 m. The chambers had inactive holes through their centers, where the beam tube passed. The apertures of the magnet, spark chambers, and beam tube produced the acceptance shown in Fig. 3.

The apparatus was triggered on the detection of a scattered electron by a hodoscope of 20 scintillation counters and 11 shower counters[14] behind the second spark chamber. The shower counter thresholds were set to ~4 GeV. Photon triggers were eliminated by the requirement that a shower counter fire coincident with the scintillators in front of it. The kinematic range of inelastic electron scatters covered by this trigger was roughly $|q^2| > 0.3$ $(\mathrm{GeV}/c)^2$, $\nu < 15$ GeV. There was no hadron requirement in the trigger.

For each trigger a single picture was taken of the optical spark chambers on 70 mm film. The camera was located in the horizontal plane 21.6 m from the beam line with its optic axis aligned perpendicular to the beam. Each picture contained four views of each chamber, a direct view, a top and a bottom view in small angle stereo, and a rear view to expose tracks blocked in the direct view by a beam pipe. Figure 4 contains a picture of an event which is a candidate for an elastically produced rho meson.

A PDP-8 computer recorded scintillation and shower counter status, shower counter pulse heights, and scintillation counter timing information for each event.

The beam flux was integrated by a quantameter located behind the shower counters and was monitored instantaneously by a surface-barrier detector.[15]

IV. DATA COLLECTION AND REDUCTION

We recorded 250,000 pictures with the H_2 target corresponding to 2.6×10^{12} incident electrons. All of the film was measured by a flying-spot digitizer, Hummingbird II,[16] and selected samples were also measured by a conventional manual system.

The momentum of each reconstructed track was computed by propagating the track back through the magnet and adjusting the momentum until the track intercepted the target vertically. Tracks which did not, then, strike the target horizontally were rejected. The rms momentum resolution was 2% at 10 GeV.

In each reconstructed picture, the electron was identified by matching the positions and momenta of tracks to the position and pulse height of the shower counter which triggered the event. Remaining tracks which were consistent with the scintillator hodoscope pattern were assumed to be hadrons.

The number of electrons in each q^2-s interval was corrected for geometric efficiency, measuring losses, hadron contamination (0 to 7%), and radiative effects (10 to 48%).[17] The result was the total number of virtual photon interactions in the data in that q^2-s interval, or effectively the γ^*p total cross section, $\sigma_{tot}(q^2, s)$.

Each event with 3 or more tracks was measured up to 3 times by the manual system to see whether it contained an e, π^+, π^- combination consistent with reaction (1). The missing mass squared of events with an electron and two

hadrons with dipion mass in the ρ region is shown in Fig. 5. There is a large peak at the mass squared of a proton. The width of the peak is consistent with the experimental resolution and the tail at high missing mass is due to radiation and inelastic production of ρ^o mesons. Cuts in missing mass squared were made at 0.2 and 1.6 GeV^2 and a 1-c fit was made to the events in this interval. There were 238 "rho" events surviving this process in the kinematic range $-0.25 > q^2 > -2.00$ $(GeV/c)^2$, $10 < s < 30$ $(GeV)^2$, $0 > t' > -0.7$ $(GeV/c)^2$, and $0.6 < m_{\pi\pi} < 0.9$ GeV. These events were divided into three q^2 bins whose average properties are given in Table I.

The events in each bin were fit by a maximum-likelihood technique to the form

$$\frac{d\sigma_\rho(q^2, s)}{dt'\, d\phi_e\, d\psi\, d\cos\theta} = \sigma_{tot}(q^2, s)\frac{\sigma_\rho}{\sigma_{tot}}\, be^{bt'}\, W(\phi_e, \psi, \theta) \quad . \qquad (9)$$

The fitting function contained the normalization $\sigma_{tot}(q^2, s)$ determined by counting electrons and the detailed dependence of the geometric efficiency on the independent variables q^2, s, t, ϕ_e, ψ, cos θ. The output from the fit included the ratio of the virtual photoproduction cross section for ρ production to the total virtual photoproduction cross section, σ_ρ/σ_{tot}, the slope parameter b, and parameters from the angular correlation term, W, to be described later.

The normalized cross section, σ_ρ/σ_{tot}, was corrected for elastic ρ losses due to radiation,[18] the missing mass cut, the $m_{\pi\pi}$ cut, scanning and measuring losses, and numerous small instrumental effects. A correction was also made for the number of $\pi\pi$ events in the $m_{\pi\pi}$ interval used which were not elastic ρ events. These corrections are tabulated in Table II along with an estimate of the uncertainty in each. The overall systematic uncertainty in σ_ρ/σ_{tot} is

estimated to be 16%. The error bars indicated in the figures represent statistical errors only.

V. RESULTS FOR ρ^0 ELECTROPRODUCTION

A. Mass Spectra

Figure 6 shows the invariant mass distribution of all pion pairs consistent with the hypothesis of reaction (1). The dipion mass spectrum is dominated by the ρ^0 meson with little or no background. Some of the events with dipion mass less than .4 GeV are consistent with the hypothesis

$$\begin{array}{l} \gamma^* p \rightarrow \phi p \\ \qquad\quad \big\lfloor \rightarrow k^+ k^- \end{array} \quad . \tag{10}$$

These events will be discussed in Section VI.

In experiments conducted at lower center-of-mass energies, there is some difficulty in separating the ρp and $\pi\Delta$ final states.[5] This source of background is not present in this experiment because 1) the $\pi\Delta$ cross section falls as s^{-2} while the ρp cross section is relatively constant in s;[19] 2) the overlap region in the Dalitz plot between the ρp and $\pi\Delta$ final states decreases with increasing s; and 3) the experimental acceptance for this region of the Dalitz plot is small. This is shown in Fig. 7, where the $\pi^+ p$ invariant mass has been plotted for the "rho" events. There are no events at the mass of the Δ^{++}.

To study possible changes in the ρ^0 mass spectrum as a function of q^2, we fit the data in the range $0.44 < m_{\pi\pi} < 1.04$ GeV in each q^2 bin to the form

$$\frac{d\sigma}{dm_{\pi\pi}} = \left(\frac{m_\rho^2}{m_{\pi\pi}^2} \right)^{n/2} B(m_{\pi\pi}) \tag{11}$$

where $B(m_{\pi\pi})$ is relativistic p-wave Breit-Wigner shape[20]:

$$B(m_{\pi\pi}) = \frac{2}{\pi} \frac{m_\rho m_{\pi\pi} \Gamma(m_{\pi\pi})}{\left(m_\rho^2 - m_{\pi\pi}^2\right)^2 + m_\rho^2 \Gamma^2(m_{\pi\pi})} \tag{12}$$

where

$$\Gamma(m_{\pi\pi}) = \Gamma_0 \left(\frac{q_{\pi\pi}}{q_\rho}\right)^3 \frac{m_\rho}{m_{\pi\pi}} \tag{13}$$

and

$$q = \frac{1}{2}\left(m^2 - 4m_\pi^2\right)^{1/2} \quad . \tag{14}$$

The mass ($m_\rho = .77$ GeV) and width ($\Gamma_0 = .145$ GeV) were fixed at photoproduction values.[21] The photoproduction data were fit in an identical manner. All of the data were fit well by Eq. (4). When a flat background term was added to Eq. (11), the fit values of n did not change appreciably and backgrounds selected by the fits were between 0 and 5%. The fit values of n are shown in Fig. 8. The rho mass shape appears to become more "normal" as $|q^2|$ increases. This effect was predicted by a diffraction-dissociation model,[22] but the prescription given by that model,

$$\left(\frac{m_\rho^2}{m_{\pi\pi}^2}\right)^{n/2} \longrightarrow \left(\frac{m_\rho^2 - q^2}{m_{\pi\pi}^2 - q^2}\right)^{n/2} \tag{15}$$

provides a more drastic change in the rho mass spectrum for $|q^2| \lesssim m_\rho^2$ than is indicated by the data.

B. Momentum Transfer Distributions

We fit the t' distributions to the form $e^{bt'}$ in the range $0 > t' > -.7$ $(\text{GeV/c})^2$ in each of the q^2 bins. All of the data were fit well by this form. The results of these fits are shown in Fig. 9 along with photoproduction results,[21, 23]

which have been analyzed in the same manner as our data. The b parameter appears to decrease with increasing $|q^2|$.

The DESY streamer chamber[5] and SLAC hybrid bubble chamber[6] experiments also indicate a decrease in the b parameter with increasing $|q^2|$. Reported values of the b parameter from these experiments are generally lower than those from this experiment and this is presumably accounted for by the difference in average center-of-mass energies. To try to remove the variation in s, in Fig. 10 we have plotted the ratio of the electroproduction b parameters to the photoproduction values at the same value of s. When viewed in this way, the results of all three experiments are in reasonable agreement.

Another approach to understanding the momentum transfer distributions as a function of q^2 and s has been proposed by Nieh.[24] He presents a physical picture in which the effective size of the photon is related to the amount of time, Δt, that an associated hadronic system can exist. Δt is calculated using the uncertainty principle. In electroproduction of ρ^0 mesons,

$$\Delta t \approx \frac{2\nu}{m_\rho^2 - q^2} \tag{16}$$

and the b parameter should be a function of Δt only. The data are in qualitative agreement with this approach.

We have also determined the t' distribution separately for longitudinally and transversely polarized ρ^0 mesons and have found no significant difference between them.

C. Angular Distributions

The decay distribution of the rho meson serves as an analyzer of its polarization. Thus the correlations between the production and decay angles can yield information on the production mechanism. The complete angular

distributions have been given by Dieterle.[25] In his notation,

$$W(\phi_e, \theta, \phi) = \sum_{\substack{\lambda\lambda' \\ \sigma\sigma'}} B^{\lambda\lambda'}(\epsilon, \phi_e)\, \rho^{\lambda\lambda'}_{\sigma\sigma'}\, A_{\sigma\sigma'}(\theta, \phi) \qquad (17)$$

where $B^{\lambda\lambda'}$ is the photon density matrix, $A_{\sigma\sigma'}$ is the rho decay matrix, $\rho^{\lambda\lambda'}_{\sigma\sigma'}$ is the production matrix, and the summation is taken over the photon helicities (λ, λ') and the rho helicities (σ, σ'). $B^{\lambda\lambda'}$ and $A_{\sigma\sigma'}$ are known functions and $\rho^{\lambda\lambda'}_{\sigma\sigma'}$ is, in principle, to be determined from experiment. The production matrix has 81 elements, but parity conservation and hermiticity reduce the number of independent elements to 25.

We have studied the angular correlations in the data for evidence of non-helicity-conserving amplitudes (production matrix elements for which $\lambda \neq \sigma$ or $\lambda' \neq \sigma'$) and have failed to find any at the 10% level, the statistical level of this experiment. Thus we have assumed that s-channel helicity conservation holds in electroproduction, as it does in photoproduction.[21] In this case Eq. (17) reduces to

$$W(\theta, \psi) = \frac{3}{8\pi^2(1+\epsilon R_\rho)}\left[\epsilon R_\rho \cos^2\theta + \frac{1}{2}\sin^2\theta\,(1+\epsilon\cos 2\psi) - (\epsilon R_\rho(1+\epsilon)/2)^{\frac{1}{2}}\cos\delta\,\sin 2\theta\,\cos\psi\right], \qquad (18)$$

where R_ρ is the ratio for the production of longitudinally to transversely polarized ρ^0 mesons and δ is the phase angle between the longitudinal and transverse amplitudes. The results of the fits for R_ρ and $\cos\delta$ are given in Figs. (11a) and (11b).

We have fit R_ρ to the form suggested by the VMD model of Sakurai and Schildknecht,[10]

$$R_\rho = -\xi^2\,\frac{q^2}{m_\rho^2} \quad . \qquad (19)$$

The data are adequately described by this fit with $\xi^2 = .45^{+.15}_{-.10}$. However, this value of ξ^2 is not consistent with the value required by their model to fit inelastic electron scattering results, $\xi^2 \approx .06$.

Eckardt et al.[5] report a value of $R_\rho = .30 \pm .14$ at $\langle q^2 \rangle = -.6$ (GeV/c)^2 and $\langle s \rangle = 5.3$ GeV^2. Preliminary results for R_ρ from the SLAC hybrid bubble chamber experiment are in excellent agreement with our measurements.[26]

The measurements of cos δ plotted in Fig. 11b show almost maximal interference between transverse and longitudinal amplitudes. This interference term is evidenced by the clustering of events in the cos $\theta - \psi$ scatter plot (Fig. 12). Both the raw data and data approximately corrected for the geometrical acceptance are shown.

For a purely diffractive production process cos δ should be unity. Again the preliminary results of the SLAC hybrid bubble chamber experiment for cos δ are in excellent agreement with our measurements,[26] but the DESY streamer chamber experiment reports no evidence for transverse-longitudinal interference.[5]

D. Total ρ^o Cross Sections

Figure 13 shows the ratio of the ρ^o virtual photoproduction cross section to the total virtual photoproduction cross section. Photoproduction cross section ratios, which were obtained by similar analysis methods, are also shown. The ρ^o cross section drops faster than the total virtual photoproduction cross section and also faster than the prediction of the VMD model,[10]

$$\left.\frac{d\sigma_\rho(q^2)}{dt}\right|_{t=0} = \left.\frac{d\sigma_\rho(0)}{dt}\right|_{t=0} \frac{\left(1 - \epsilon\xi^2 q^2/m_\rho^2\right)}{\left(1 - q^2/m_\rho^2\right)^2} \quad , \qquad (20)$$

with $\xi^2 = .45$. We note, however, that the data can be described by the simple form,

$$\sigma_\rho(q^2) = \sigma_\rho(0) \frac{e^{bt_{min}}}{\left(1 - q^2/m_\rho^2\right)^2} \quad . \tag{21}$$

Both Eqs. (20) and (21) are displayed in Fig. 13 in terms of cross section ratios. The $e^{bt_{min}}$ factor in Eq. (21) is relatively unimportant, contributing only 15% for the highest $|q^2|$ bin.

There is a general experimental agreement that the ρ^o virtual photoproduction cross section falls substantially faster than the total virtual photoproduction cross section as $|q^2|$ increases.[4-6]

All of our results for ρ^o production are summarized in Table III.

VI. ϕ ELECTROPRODUCTION

The data reduction procedure was repeated for electron and two hadron combinations with the assumption that the hadrons were K mesons. Figure 14 shows the dikaon mass distribution for events consistent with the hypothesis

$$\gamma^* p \rightarrow K^+ K^- p \quad . \tag{22}$$

There are six events at the mass of the ϕ meson. We estimate that the background from electron, muon, and pion pairs is 1 ± 1 event. The average q^2 of the events is $-.6$ $(GeV/c)^2$ and the average s is 22.9 GeV^2. The acceptance for ϕ's was 60% larger than that for ρ^o's; the corrections were similar except for meson mass cut, k decay, and unseen decay modes. These corrections are tabulated in Table IV.

The ratio of the ϕ virtual photoproduction cross section to the total virtual photoproduction cross section is $.0017 \pm .0009$ compared to $.0046 \pm .0006$ for photoproduction.[21]

VII. UNITARITY LOWER BOUND ON THE LONGITUDINAL TO TRANSVERSE RATIO FOR THE TOTAL VIRTUAL PHOTOPRODUCTION CROSS SECTION

With only a few very reasonable assumptions, we can derive a nontrivial lower bound on the longitudinal to transverse ratio for the total virtual photoproduction cross section from our measurements of ρ^0 electroproduction. We will refer to this ratio as R_{tot} to distinguish it from R_ρ, the longitudinal to transverse ratio for ρ^0 electroproduction. At higher values of $|q^2|$, R_{tot} has been determined by single-arm electron scattering experiments[27] and is conventionally given by

$$R_{tot} = \left(1 - \frac{\nu^2}{q^2}\right) \frac{W_2}{W_1} - 1 \tag{23}$$

in terms of the usual structure functions.

The formalism, an "optical theorem for quasi-elastic scattering," was first given by Knies who applied it to predict a lower bound on the total (real) photoproduction cross section based on measurements of ρ^0 photoproduction.[28] Recently Sakurai has applied it to electroproduction[29] using some preliminary data. The only theoretical inputs are the unitarity relation and the Schwarz inequality. No assumption of VMD is needed.

Given any two-body inelastic reaction $a \to b$, then from Eq. (5.3) of Ref. 28,

$$h(a,b) \frac{d\sigma'}{dt}(a \to b)\Big|_{\theta=0} \leq \frac{1}{16\pi} \sigma_{tot}(a)\, \sigma_{tot}(b) \tag{24}$$

where $d\sigma'/dt$ indicates the part of the cross section which comes from the imaginary part of the scattering amplitude, and $h(a,b)$ is a kinematical factor required by the reciprocity relation. We rewrite Eq. (24) for the case in which

$a = \gamma^* p$ and $b = \rho^o p$, both in the longitudinal helicity state,

$$\sigma_L(\gamma^* p) \geq \frac{16\pi}{\sigma_L(\rho^o p)} \, h \frac{d\sigma'}{dt} (\gamma^* p \to \rho^o p)_L \Big|_{t=t_{min}} \tag{25}$$

where

$$h = \left[\frac{(s - q^2 - m^2)^2 - 4q^2 m^2}{\left(s - m_\rho^2 - m^2\right)^2 - 4m_\rho^2 m^2} \right]^{\frac{1}{2}} . \tag{26}$$

To evaluate Eq. (25) we need three assumptions:

(1) The forward ρ^o electroproduction cross section comes from the imaginary part of the scattering amplitude. This assumption is supported by lack of strong s dependence in the cross section, the lack of evidence for non-helicity-conserving amplitudes, and the near maximal transverse-longitudinal interference term.

(2) The momentum transfer distributions are the same for transverse and longitudinal ρ^o production. As we noted in Section III.B, there is no evidence to the contrary.

(3) The longitudinal $\rho^o p$ total cross section is less than or equal to the transverse $\rho^o p$ cross sections as determined by photoproduction of ρ^o mesons from complex nuclei. VMD models[8] would predict $\sigma_L(\rho^o p) < \sigma_T(\rho^o p)$ since they identify

$$(\xi^2)^{\frac{1}{2}} = \frac{\sigma_L(\rho^o p)}{\sigma_T(\rho^o p)} \tag{27}$$

where ξ^2 is determined experimentally by Eq. (19). We take $\sigma_L(\rho^o p) = \sigma_T(\rho^o p) = 27.5$ mb.[30]

Using these assumptions and the values in Table III it is straight forward to evaluate $\sigma_L(\gamma^* p)$ from Eq. (25) and correspondingly R_{tot}. At the one standard

deviation level, the lower bounds for R_{tot} are .045, .079, and .001 corresponding to the $q^2 = -.36$, $-.70$, and -1.27 $(GeV/c)^2$ bins. These values are plotted in Fig. 15 along with the highest s values ($10.9 \leq s \leq 16.0$ GeV^2) of R_{tot} determined by Miller et al.[27]

As Sakurai has emphasized,[29] these lower bounds on R_{tot} rule out the form

$$R_{tot} = -q^2/\nu^2 \tag{28}$$

in our kinematic region, but are consistent with

$$R_{tot} = \text{constant} = .18 \quad . \tag{29}$$

Equation (29) cannot be correct at all q^2, however, since $R_{tot} \to 0$ as $|q^2| \to 0$.

VIII. CONCLUSIONS

We have measured the reaction $\gamma^* p \to \rho^o p$ as a function of the γ^* mass squared q^2 and have observed the following behavior:

(1) The dipion mass spectrum becomes more "normal" as $|q^2|$ increases.

(2) The momentum transfer distribution broadens as $|q^2|$ increases indicating a shrinking of the photon in some theoretical treatments.[24]

(3) There is no evidence for s-channel helicity nonconservation. The production of longitudinally polarized ρ^o mesons increases with $|q^2|$ at a much larger rate than can be accommodated by a VMD model interpretation of deep inelastic electron scattering.[10] The interference between transverse and longitudinal amplitudes is almost maximal.

(4) The cross section decreases with $|q^2|$ roughly as the ρ^o propagator squared, $\left(1 - q^2/m_\rho^2\right)^{-2}$.

We have also observed that the cross section for $\gamma^* p \to \phi p$ decreases with $|q^2|$.

We have calculated lower bounds on the longitudinal-transverse ratio, R_{tot}, inelastic electron scattering and have concluded that $R_{tot} >> -q^2\nu^{-2}$ in our kinematic region.

ACKNOWLEDGMENTS

We wish to acknowledge the technical support contributed by numerous SLAC groups, particularly the cooperation from Steve St. Lorant and the Low Temperature group, and John Brown and the Data Analysis group.

Byron Dieterle and Benson T. Chertok provided valuable assistance in the early stages of the experiment.

We are indebted to C. A. Lichtenstein and to W. Atwood and S. Stein for supplying us with computer programs for the evaluation of radiative corrections. We are grateful to D. Schildknecht for illuminating discussions on aspects of the VMD model.

REFERENCES

1. J. T. Dakin, G. J. Feldman, W. L. Lakin, F. Martin, M. L. Perl, E. W. Petraske, and W. T. Toner, Phys. Rev. Letters 30, 142 (1973).
2. D. E. Andrews, K. Berkelman, D. G. Cassel, D. L. Hartill, J. Hartmann, R. Kerchner, E. Lazarus, R. M. Littauer, R. L. Loveless, R. Rohlfs, D. H. White, and A. J. Sadoff, Phys. Rev. Letters 26, 864 (1971).
3. E. D. Bloom, R. L. A. Cottrell, H. DeStaebler, C. L. Jordan, G. Miller, H. Piel, C. Prescott, R. Siemann, C. K. Sinclair, S. Stein, and R. E. Taylor, Phys. Rev. Letters 28, 516 (1972).
4. C. Driver, K. Heinloth, K. Hohne, G. Hofmann, F. Janata, P. Karow, D. Schmidt, G. Specht, and J. Rathje, Nucl. Phys. B38, 1 (1972), and erratum (to be published).
5. V. Eckardt, H. J. Gebauer, P. Joos, H. Meyer, B. Naroska, D. Notz, W. J. Podolsky, G. Wolf, S. Yellin, H. Dau, G. Drews, D. Greubel, W. Meincke, H. Nagel, and E. Rabe, DESY Report No. 72/67 (1972) (to be published).
6. J. Ballam, E. D. Bloom, J. T. Carroll, G. B. Chadwick, R. L. A. Cottrell, M. Della Negra, H. DeStaebler, L. K. Gershwin, L. P. Keller, M. D. Mestayer, K. C. Moffeit, C. Y. Prescott, and S. Stein, SLAC Report No. SLAC-PUB-1163 (1972) (unpublished).
7. H. Fraas and D. Schildknecht, Nucl. Phys. B14, 543 (1969).
8. C. F. Cho and G. J. Gounaris, Phys. Rev. 186, 1619 (1969).
9. G. Kramer and H. R. Quinn, DESY Report No. 72/23 (1972) (to be published); G. Preparata, Phys. Letters 36B, 53 (1971); M. Sakuraoka, Lettere Nuovo Cimento 3, 89 (1972).

10. J. J. Sakurai and D. Schildknecht, Phys. Letters 40B, 121 (1972), Phys. Letters 41B, 489 (1972), and Phys. Letters 42B, 216 (1972).

11. N. Dombey, Rev. Mod. Phys. 41, 236 (1969).

12. L. N. Hand, Phys. Rev. 129, 1834 (1963).

13. F. Martin, S. J. St. Lorant, and W. T. Toner, Nucl. Instr. and Methods 103, 503 (1972); A. C. Newton, F. Martin, S. J. St. Lorant, and W. T. Toner, SLAC Report No. SLAC-PUB-1102 (1972) (to be published); and F. Martin and S. J. St. Lorant, J. Appl. Phys. 44, 460 (1973).

14. W. L. Lakin, E. W. Petraske, and W. T. Toner, Nucl. Instr. and Methods 103, 431 (1972).

15. W. L. Lakin, R. E. Baggs, Nucl. Instr. and Methods 102, 367 (1972).

16. J. L. Brown, SLAC Report No. SLAC-PUB-752 (1970) (unpublished).

17. G. Miller, SLAC Report No. SLAC-129 (1971) (unpublished).

18. A. Bartl and P. Urban, Acta Physica Austrica 24, 139 (1966).

19. I. Dammann, C. Driver, K. Heinloth, G. Hofmann, F. Janata, P. Karow, D. Luke, D. Schmidt, and G. Specht, DESY Report No. 72/70 (1972) (to be published).

20. J. D. Jackson, Nuovo Cimento 34, 1645 (1964).

21. J. Ballam, G. B. Chadwick, Y. Eisenberg, E. Kogan, K. C. Moffeit, P. Seyboth, I. O. Skillicorn, H. Spitzer, G. Wolf, H. H. Bingham, W. B. Fretter, W. J. Podolsky, M. S. Rabin, A. H. Rosenfeld, and G. Smadja, SLAC Report No. SLAC-PUB-1143 (1972) (to be published). We use the 9.3 GeV data only.

22. M. Ross and L. Stodolsky, Phys. Rev. 149, 1172 (1966).

23. F. Bulos, W. Busza, R. Giese, E. Kluge, R. Larsen, D.W.G.S. Leith, and S. H. Williams, Contribution to the XVI International Conference on

High Energy Physics, NAL, Batavia, Illinois, September 1972 (unpublished). We use 9 to 13 GeV data only.

24. H. T. Nieh, Phys. Letters 38B, 100 (1972). Also see H. Cheng and T. T. Wu, Phys. Rev. 183, 1324 (1969); J. D. Bjorken, J. B. Kogut, and D. E. Soper, Phys. Rev. D3, 1382 (1971); and J. B. Kogut, Phys. Rev. D5, 1152 (1972).

25. B. Dieterle, Nuovo Cimento 11A, 523 (1972).

26. K. C. Moffeit (private communication).

27. G. Miller, E. D. Bloom, G. Buschhorn, D. H. Coward, H. DeStaebler, J. Drees, C. L. Jordan, L. W. Mo, R. E. Taylor, J. I. Freidman, G. C. Hartmann, H. W. Kendall, and R. Verdier, Phys. Rev. D5, 528 (1972).

28. G. Knies, Phys. Letters 27B, 288 (1968).

29. J. J. Sakurai, Phys. Rev. Letters 30, 245 (1973). This application was first brought to our attention by J. J. Sakurai in a seminar he gave at SLAC in December 1971.

30. See K. Gottfried, in Proceedings of the Fifth International Symposium on Electron and Photon Interactions at High Energies, Ithaca, New York, 1971, edited by N. B. Mistry (Cornell University Press, Ithaca, New York, 1972).

TABLE I

AVERAGE PROPERTIES OF THE THREE BINS IN q^2

	$-.25 > q^2 - .5$	$-.5 > q^2 - 1.0$	$-1.0 > q^2 > -2.0$	$(GeV/c)^2$
$<q^2>$	-.36	-.70	-1.27	$(GeV/c)^2$
$<s>$	22.6	19.6	19.8	GeV^2
$<\epsilon>$	.67	.74	.72	
$<\nu>$	11.7	10.4	10.7	GeV
$<\omega>$ a)	63.4	29.2	16.5	
$<t_{min}>$	-.008	-.015	-.033	$(GeV/c)^2$

a) $\omega \equiv -2m\nu/q^2$

TABLE II

CORRECTION FACTORS APPLIED TO σ_ρ/σ_{tot}

The numbers in parenthesis indicate the percentage uncertainty in the indicated factor. The corrections were substantially the same for each of the q^2 bins. The 16% overall systematic uncertainty includes additional contributions from the electron detection efficiency, the radiative corrections to σ_{tot} and knowledge of the acceptance.

Missing mass cuts	1.09	(4)
Radiative effects	1.24	(5)
Scanning losses	1.05	(5)
Measuring losses	1.05	(5)
Counter positions and deadtime	1.04	(2)
Pion decay in flight	1.02	(0)
Pion absorption	1.01	(0)
Ambiguous events	1.04	(0)
Background	.95	(5)
Dipion mass cuts	1.29	(7)
TOTAL	2.04	(16)

TABLE III

ρ^0 ELECTROPRODUCTION RESULTS

The errors are statistical only.

$\langle q^2 \rangle$		-.36	-.70	-1.27	$(GeV/c)^2$
n	(Eq. (11))	$4.8 \pm .7$	$3.5 \pm .9$	1.0 ± 1.7	
b	(Eq. (9))	7.9 ± 1.0	$6.9 \pm .7$	4.8 ± 1.0	$(GeV/c)^2$
R_ρ	(Eq. (18))	$.32^{+.24}_{-.18}$	$.63^{+.28}_{-.21}$	$.27^{+.52}_{-.25}$	
$\cos \delta$	(Eq. (18))	$.70^{+.24}_{-.26}$	$.75^{+.15}_{-.17}$	$.80^{+.20}_{-.48}$	
σ_ρ/σ_{tot}	(Eq. (9))	$.071 \pm .007$	$.055 \pm .005$	$.031 \pm .005$	
σ_ρ	(Eqs. (7), (9))	$4.6 \pm .5$	$2.5 \pm .2$	$.94 \pm .15$	μb

TABLE IV

CORRECTION FACTORS APPLIED TO σ_ϕ/σ_{tot}

The numbers in parenthesis indicate the percentage uncertainty in the indicated factor. The 26% overall systematic uncertainty includes additional contributions from the electron detection efficiency, the radiative corrections to σ_{tot} and knowledge of the acceptance.

Missing mass cuts	1.09	(4)
Radiative effects	1.23	(5)
Scanning losses	1.05	(5)
Measuring losses	1.05	(5)
Counter positions and deadtime	1.04	(2)
K decay in flight	1.42	(10)
K absorption	1.01	(0)
Ambiguous events	1.04	(0)
Background	.83	(20)
Dikaon mass cuts	1.00	(0)
Unseen decay modes	2.04	(2)
TOTAL	3.88	(26)

FIGURE CAPTIONS

1. Coordinate systems and angles for ρ^o electroproduction.
2. Schematic elevation view of the apparatus.
3. Geometric acceptance of the apparatus averaged over the azimuthal angle.
4. Photograph of a typical ρ-like event.
5. Missing mass squared for events with dipion mass in the range .6 to .9 GeV.
6. Dipion mass spectrum for all events in which the missing mass is consistent with that of a proton. The curve represents the relative acceptance averaged over all other variables.
7. Invariant $\pi^+ p$ mass for events which are consistent with the hypothesis of ρ^o electroproduction.
8. The parameter n defined in Eq. (11). Photoproduction data ($q^2=0$) are taken from Ref. 21.
9. The b parameter from fits to the form $e^{bt'}$. Photoproduction data ($q^2=0$) are taken from Refs. 21 and 23.
10. The ratio of electroproduction to photoproduction b parameters (from fits to the form $e^{bt'}$ or e^{bt}) at the same value of s. Data from this experiment and Refs. 5 and 6 are shown.
11. (a) The ratio of longitudinal to transverse ρ^o production. The dotted line is the best fit to Eq. (19). (b) Cosine of the longitudinal-transverse phase difference.
12. Scatter plots of the data as a function of ψ and cos θ. The top plot is of the raw data and the bottom plot is of data approximately corrected for geometrical acceptance.
13. The ratio of the ρ^o virtual photoproduction cross section to the total virtual photoproduction cross section. The solid curve represents the prediction

of the VMD model, Eq. (20), and the dashed curve represents Eq. (21). Photoproduction data ($q^2=0$), are taken from Refs. 21 and 23.

14. Dikaon spectrum for events in which the missing mass is consistent with that of a proton when all observed hadrons are assumed to be kaons.

15. Lower bounds on R_{tot}, the longitudinal-transverse ratio in inelastic electron scattering, at the one standard deviation level. The dotted cross bars indicate the lower bound at the zero standard deviation level, or alternatively the lower bound derived from the values in Table III, assuming all experimental errors are zero. The highest s value data from the single-arm experiment (Ref. 27) are also shown.

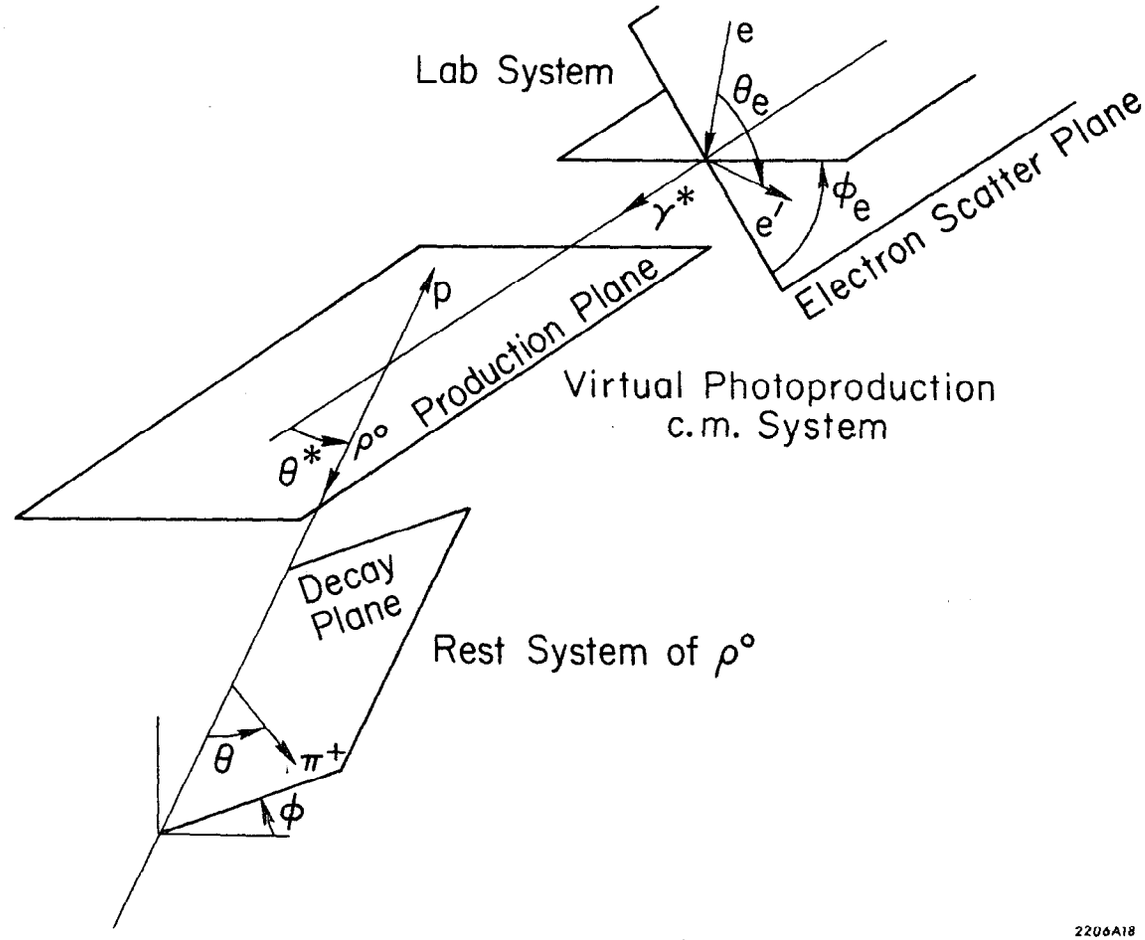
Lab System
e
θ_e
ϕ_e
e^-
γ^*
Electron Scatter Plane
p
Production Plane
Virtual Photoproduction
c.m. System
θ^*
ρ^o
Decay
Plane
Rest System of ρ^o
θ
π^+
ϕ
2206A18

Fig. 1

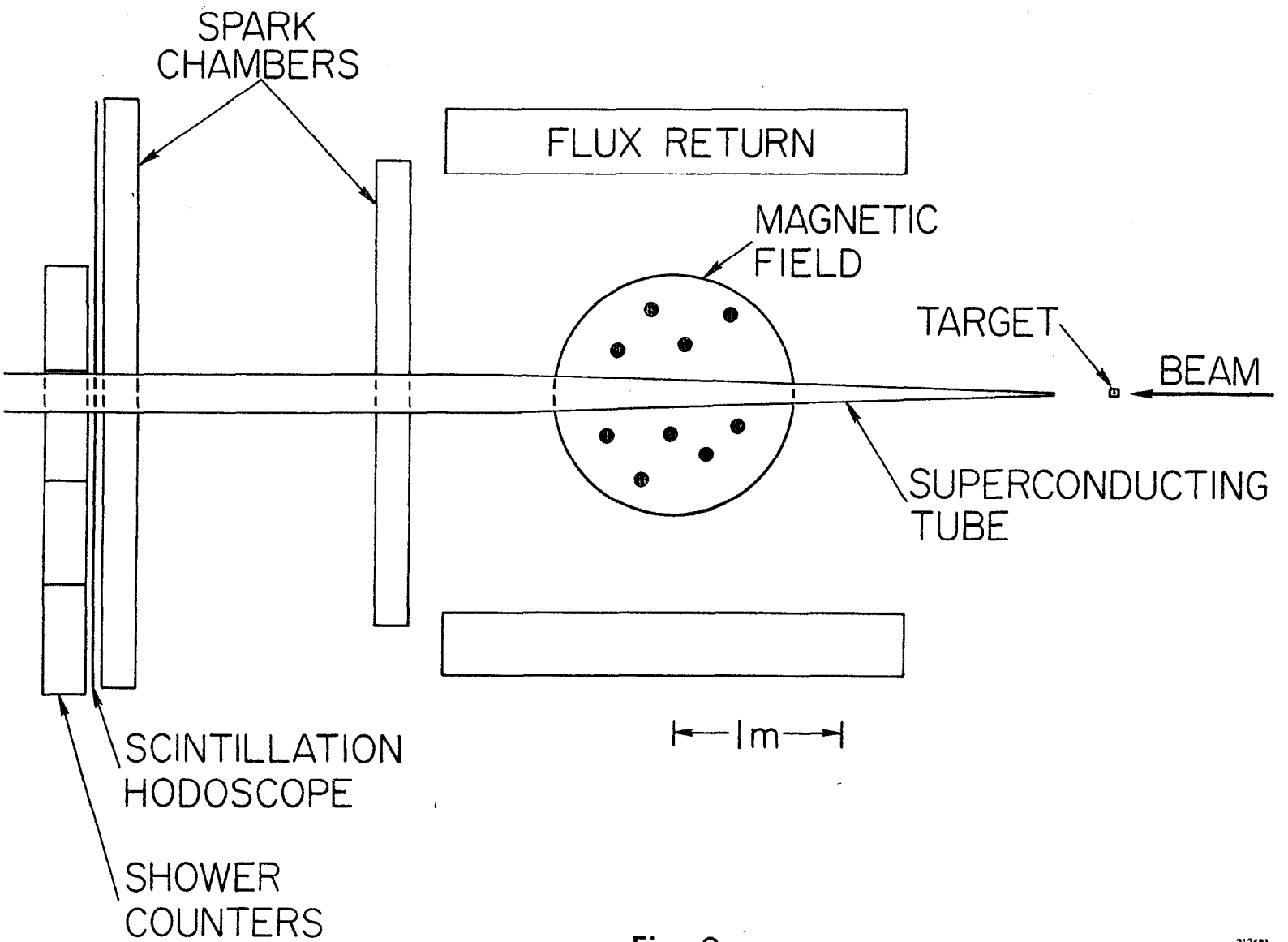
SPARK
CHAMBERS
FLUX RETURN
MAGNETIC
FIELD
TARGET
BEAM
SUPERCONDUCTING
TUBE
SCINTILLATION
HODOSCOPE
SHOWER
COUNTERS
1m

Fig. 2

212481

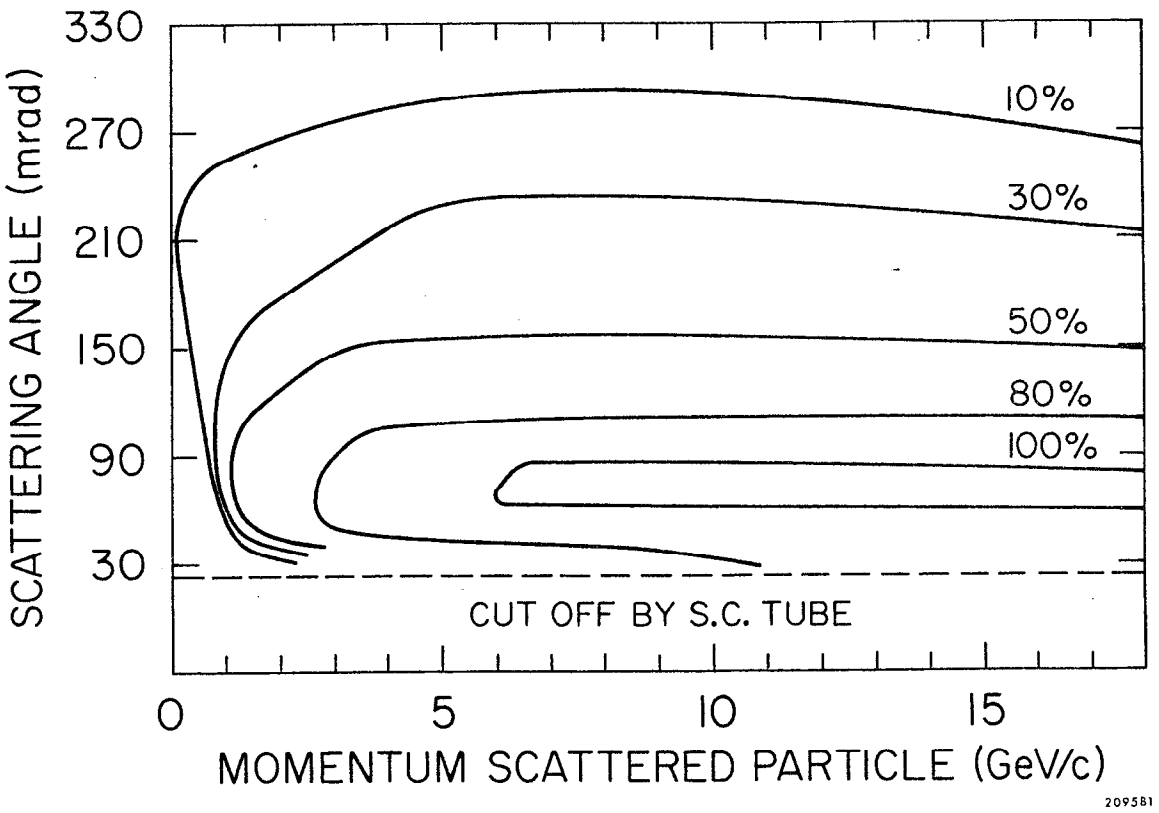
330
270
210
150
90
30
SCATTERING ANGLE (mrad)
10%
30%
50%
80%
100%
CUT OFF BY S.C. TUBE
0
5
10
15
MOMENTUM SCATTERED PARTICLE (GeV/c)
209581

Fig. 3

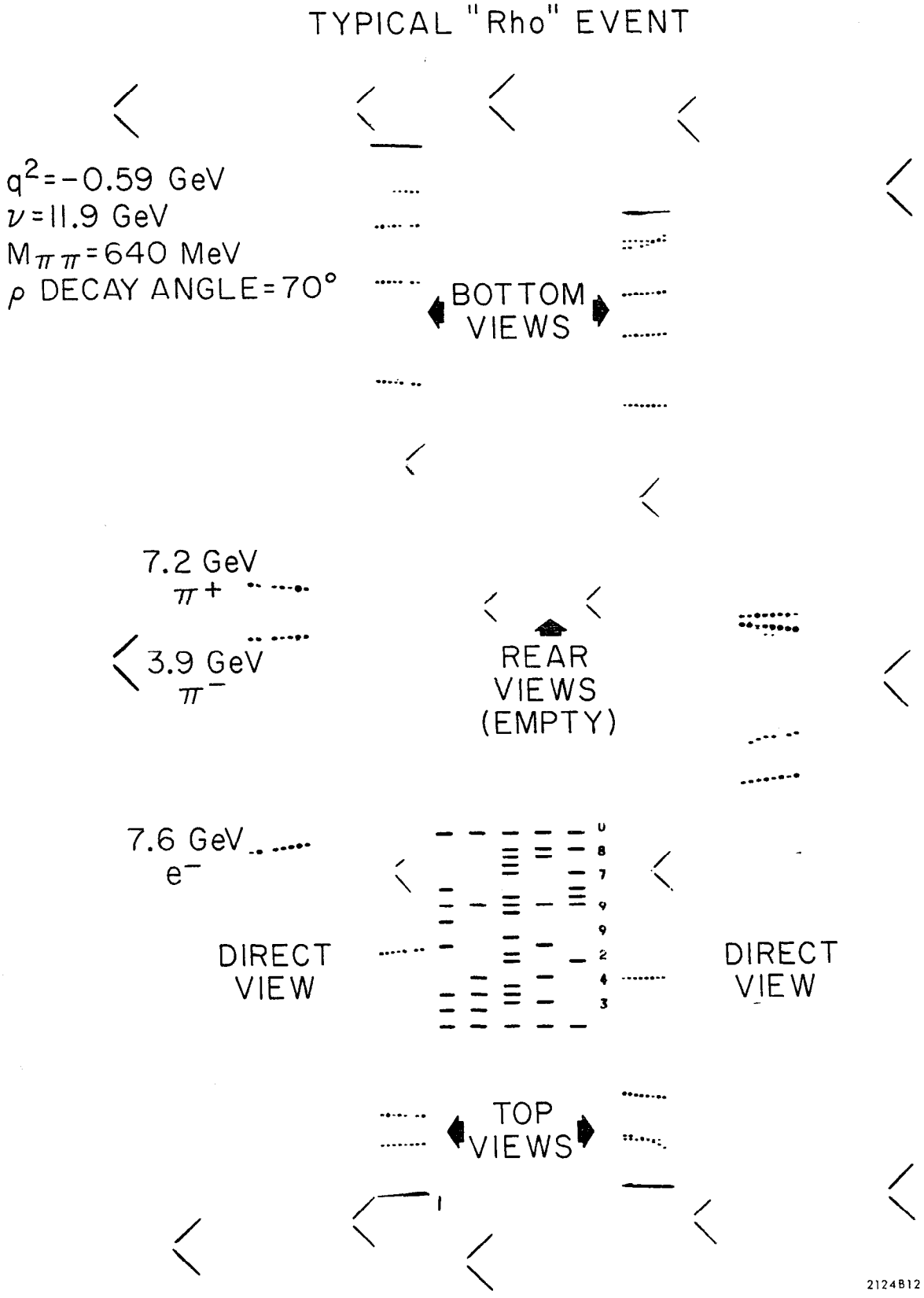
TYPICAL "Rho" EVENT
$q^2 = -0.59$ GeV
$\nu = 11.9$ GeV
$M_{\pi\pi} = 640$ MeV
ρ DECAY ANGLE = 70°
BOTTOM VIEWS
7.2 GeV π^+
3.9 GeV π^-
REAR VIEWS (EMPTY)
7.6 GeV e^-
DIRECT VIEW
DIRECT VIEW
TOP VIEWS
2124B12

Fig. 4

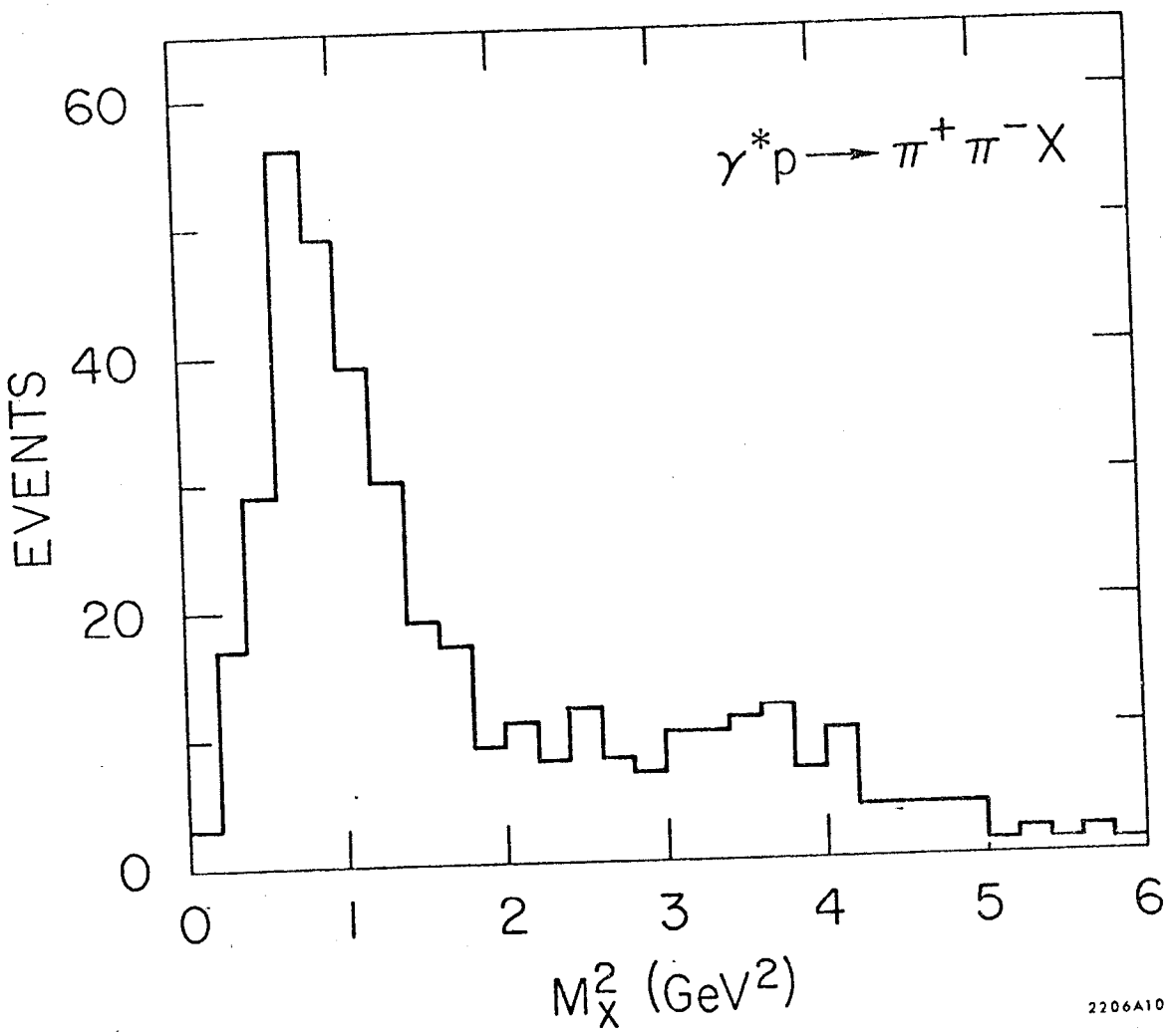
60
40
20
0
EVENTS
$\gamma^* p \rightarrow \pi^+ \pi^- X$
0
1
2
3
4
5
6
M_X^2 (GeV^2)
2206A10

Fig. 5

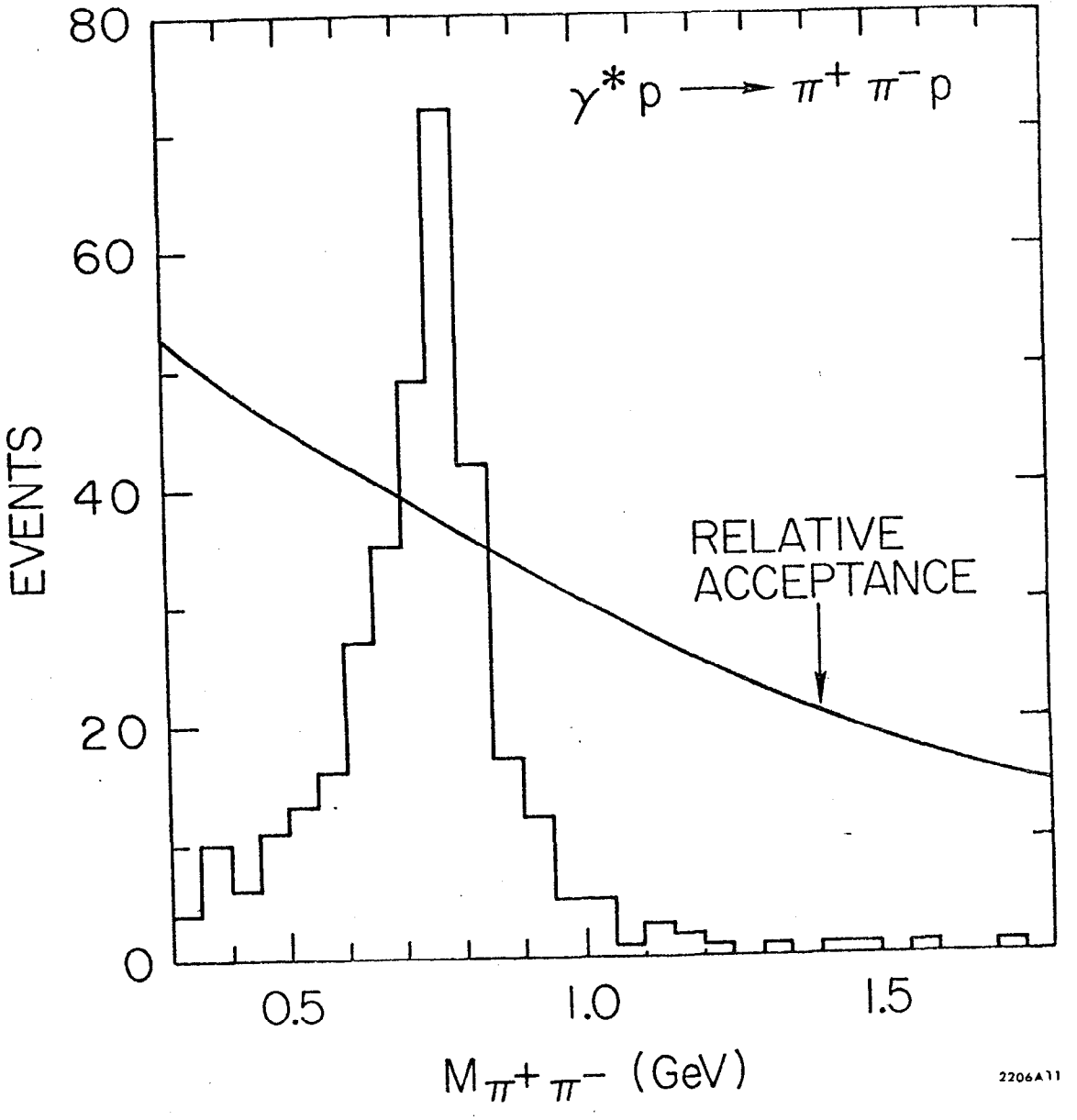
80
60
40
20
0
EVENTS
$\gamma^* p \longrightarrow \pi^+ \pi^- p$
RELATIVE
ACCEPTANCE
0.5
1.0
1.5
$M_{\pi^+\pi^-}$ (GeV)
2206A11

Fig. 6

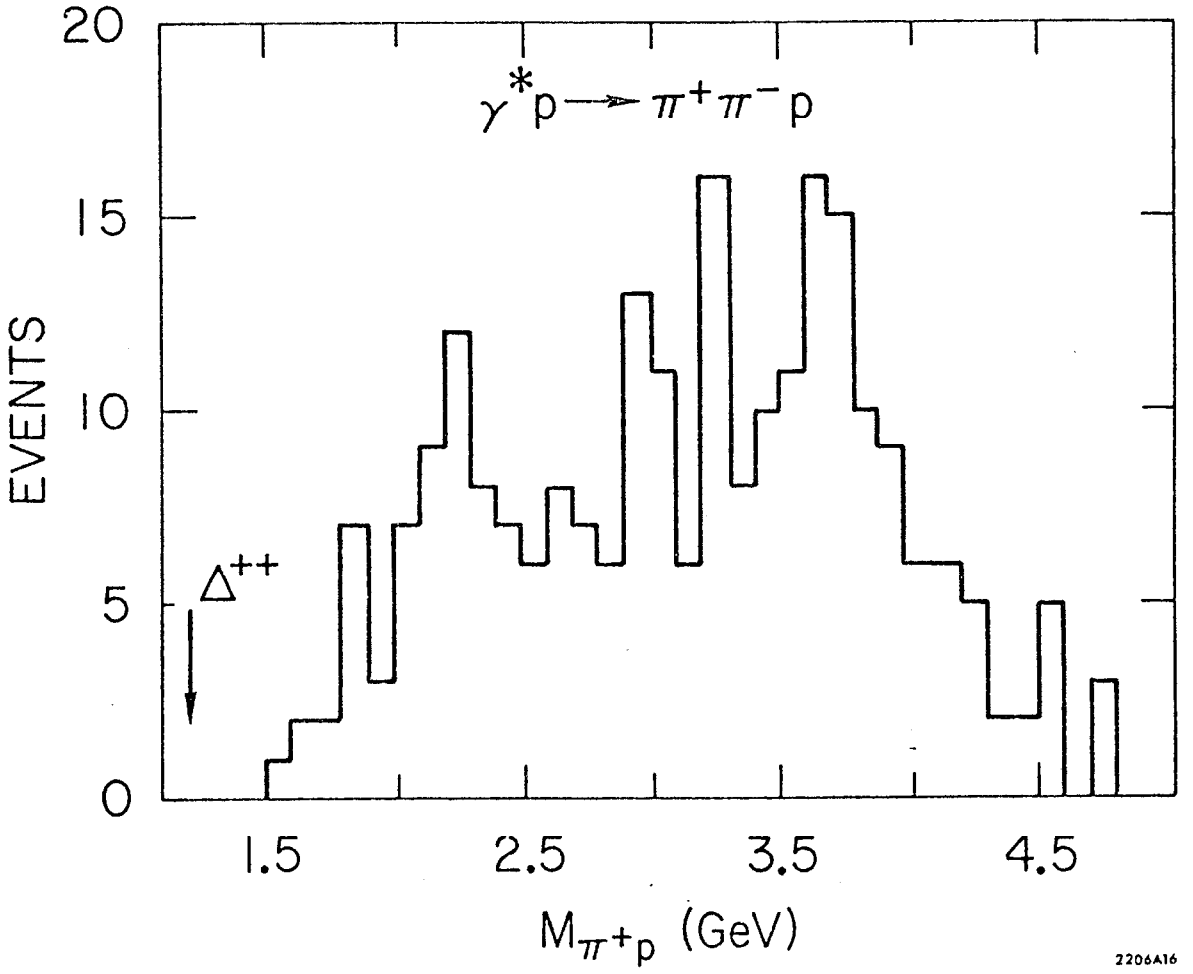
20
15
10
5
0
EVENTS
$\gamma^* p \rightarrow \pi^+ \pi^- p$
Δ^{++}
1.5
2.5
3.5
4.5
$M_{\pi^+ p}$ (GeV)
2206A16

Fig. 7

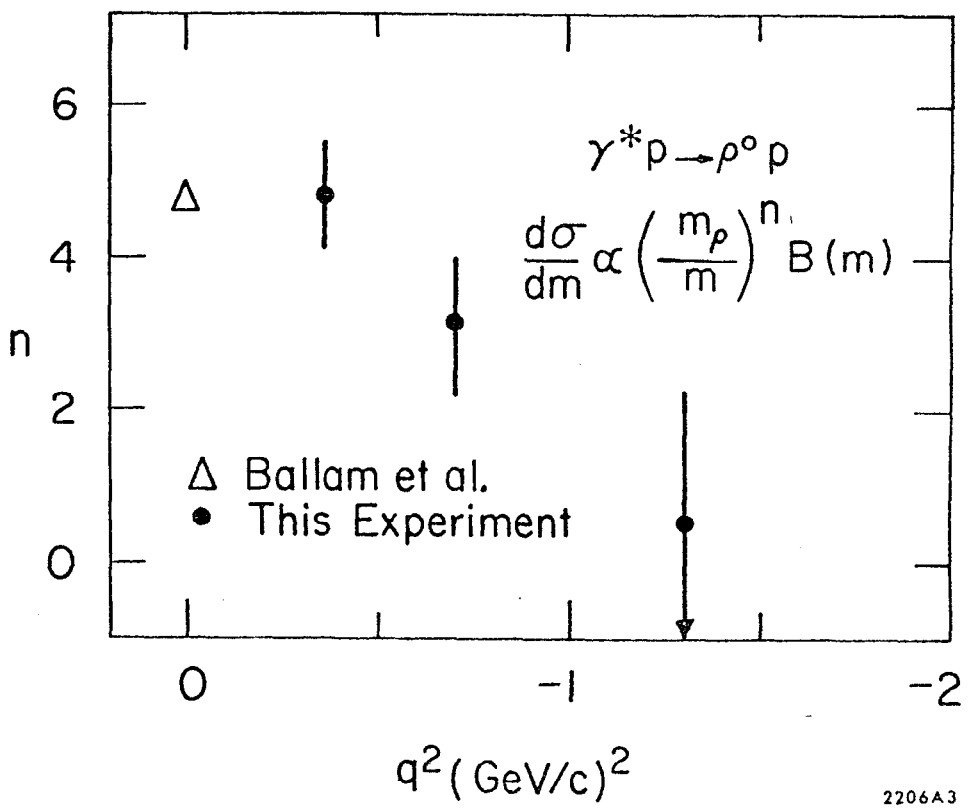
6
4
2
0
n
$\gamma^* p \to \rho^0 p$
$\frac{d\sigma}{dm} \propto \left(\frac{m_\rho}{m}\right)^n B(m)$
Δ Ballam et al.
• This Experiment
0
-1
-2
q^2 (GeV/c)^2
2206A3

Fig. 8

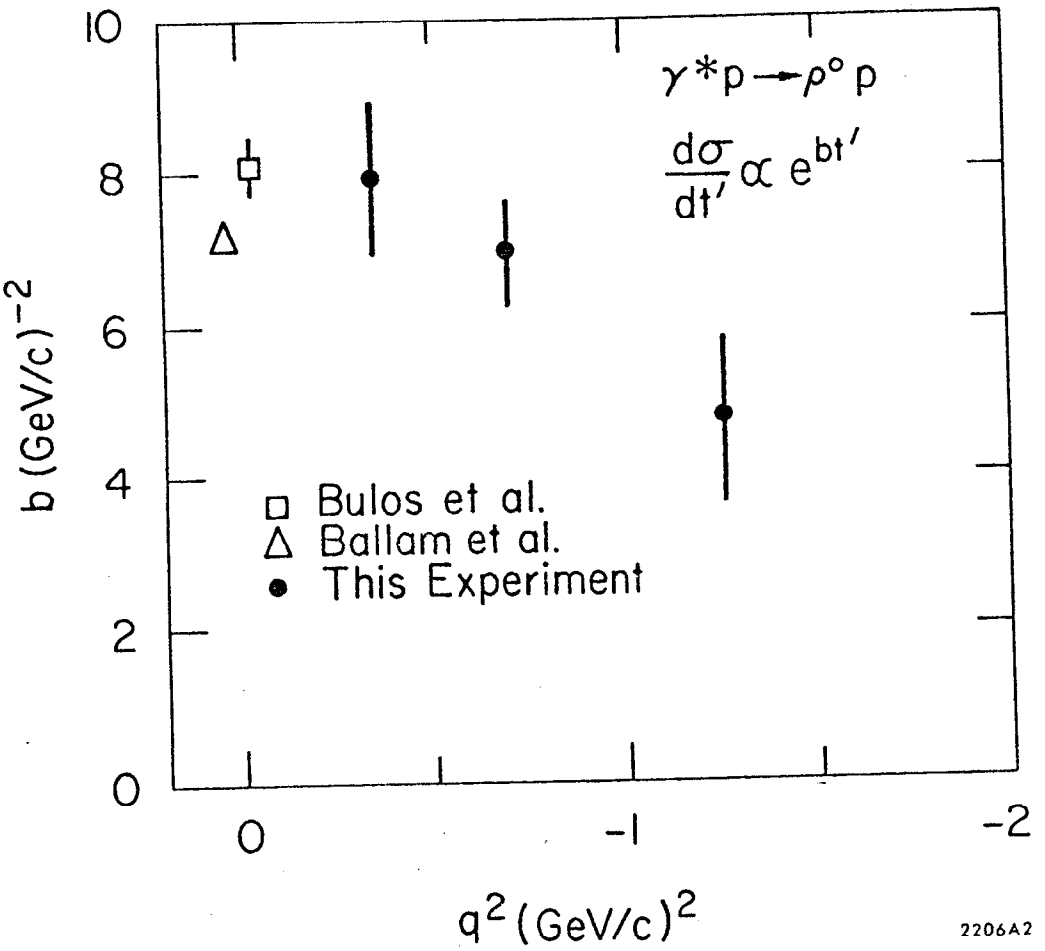
10
8
6
4
2
0
b (GeV/c)$^{-2}$
$\gamma^* p \rightarrow \rho^0 p$
$\frac{d\sigma}{dt'} \propto e^{bt'}$
Bulos et al.
Ballam et al.
This Experiment
0
-1
-2
q^2 (GeV/c)^2
2206A2

Fig. 9

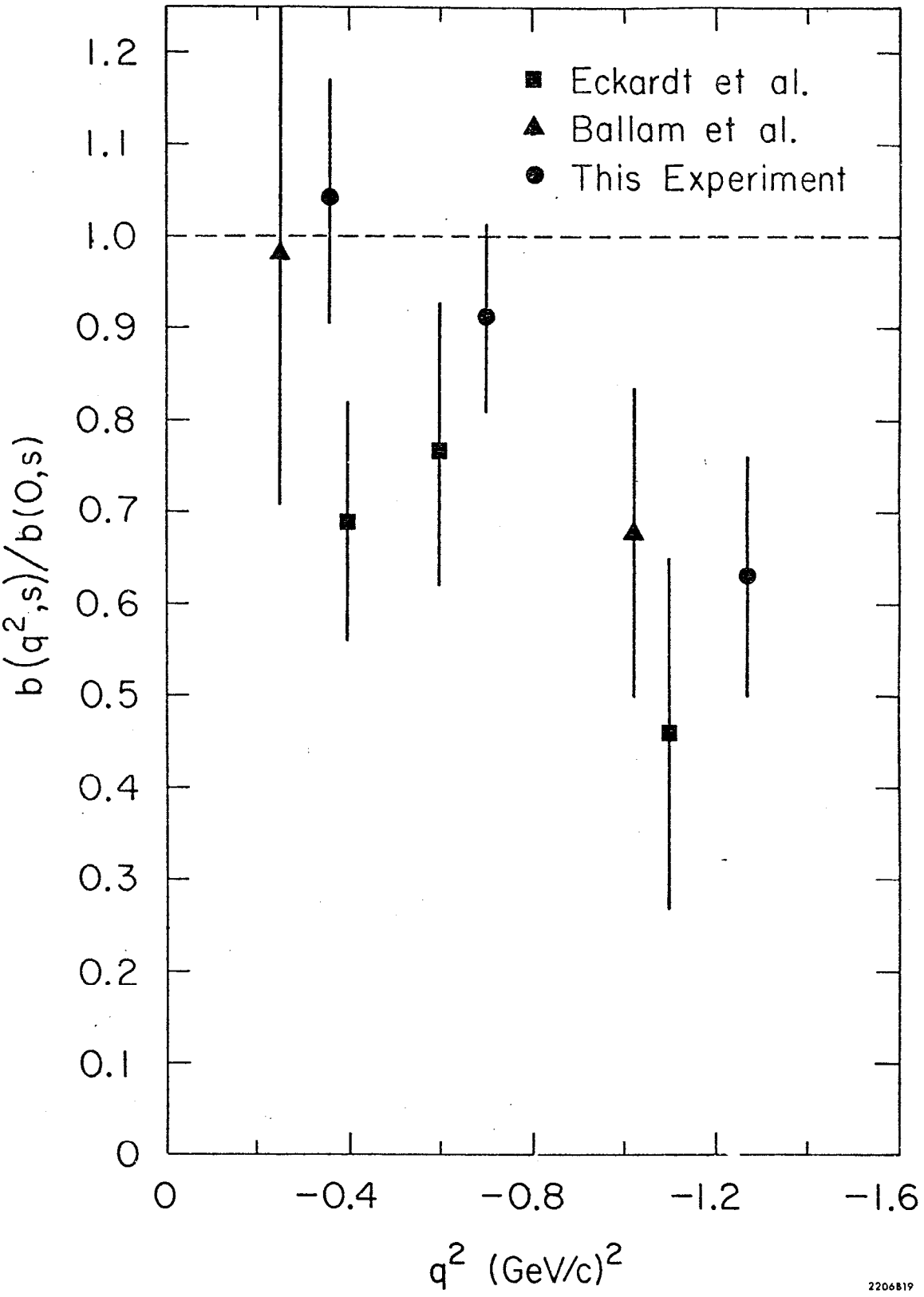
Eckardt et al.
Ballam et al.
This Experiment
b(q²,s)/b(0,s)
q² (GeV/c)²
1.2
1.1
1.0
0.9
0.8
0.7
0.6
0.5
0.4
0.3
0.2
0.1
0
0
−0.4
−0.8
−1.2
−1.6
2206B19

Fig. 10

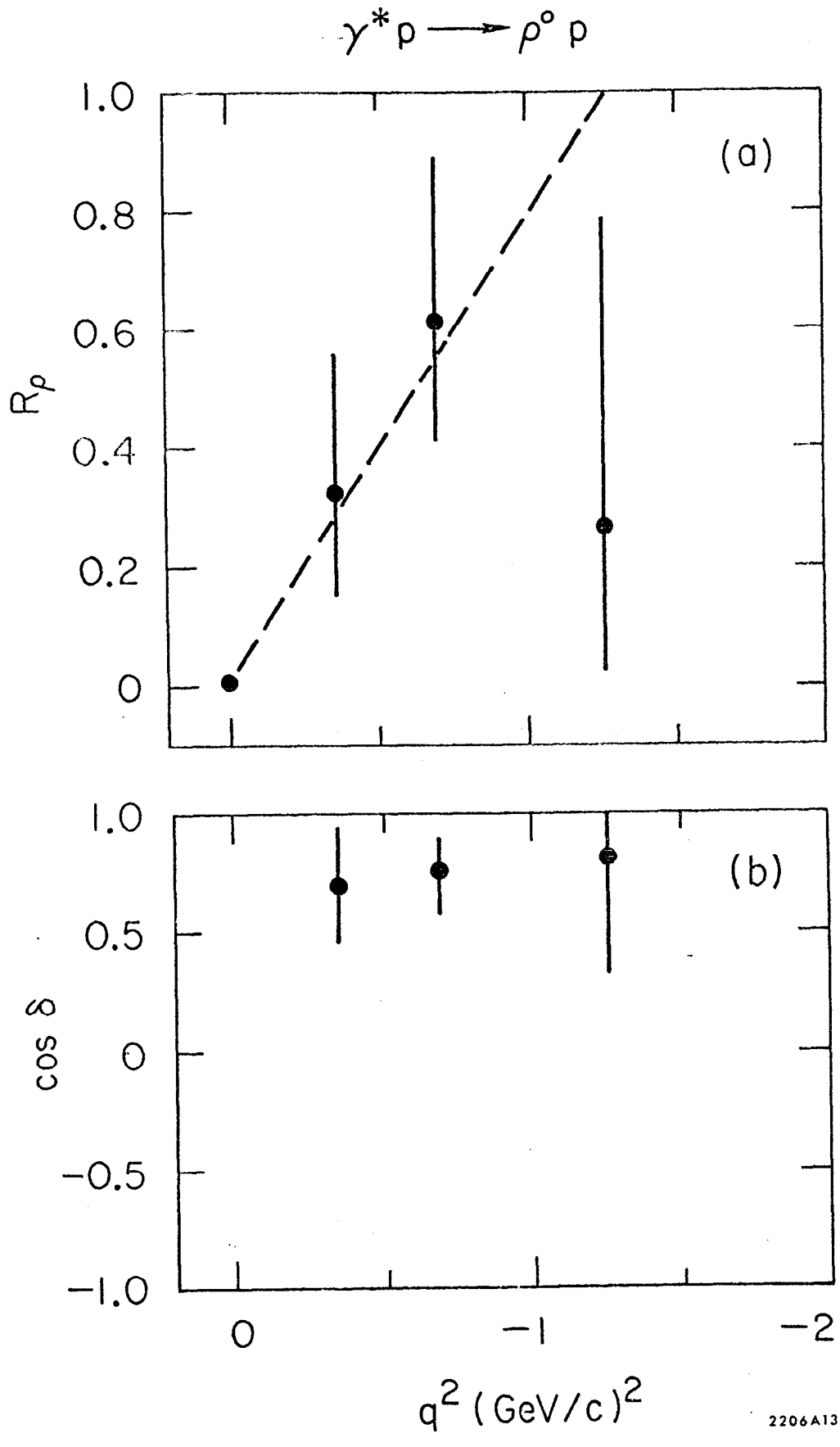
$\gamma^* p \longrightarrow \rho^0 p$
1.0
0.8
0.6
0.4
0.2
0
R_ρ
(a)
1.0
0.5
0
−0.5
−1.0
cos δ
(b)
0
−1
−2
q^2 (GeV/c)^2
2206A13

Fig. 11

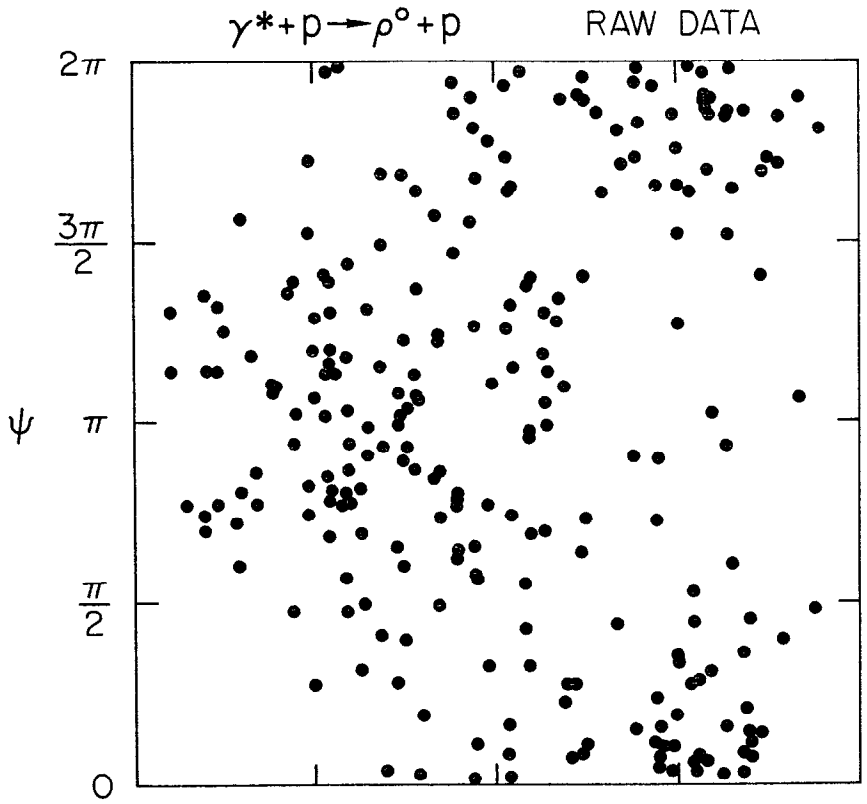
$\gamma^*+p \rightarrow \rho^0+p$
RAW DATA
2π
$\frac{3\pi}{2}$
ψ
π
$\frac{\pi}{2}$
0

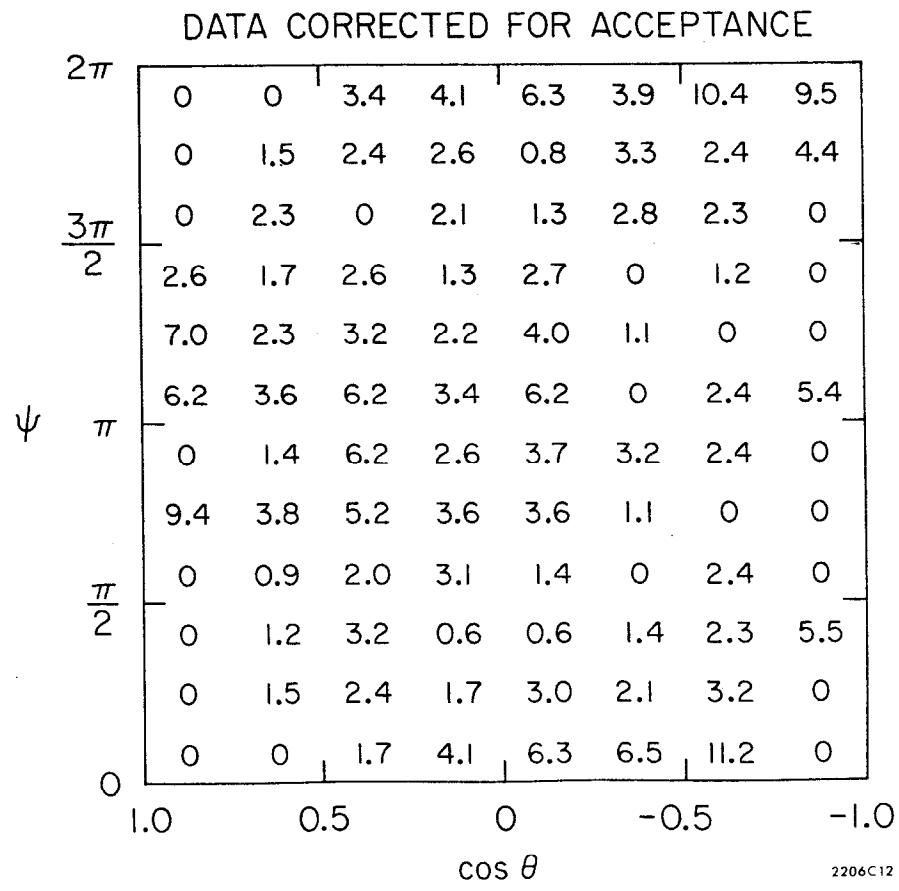
DATA CORRECTED FOR ACCEPTANCE
2π
$\frac{3\pi}{2}$
ψ
π
$\frac{\pi}{2}$
0
0 0 3.4 4.1 6.3 3.9 10.4 9.5
0 1.5 2.4 2.6 0.8 3.3 2.4 4.4
0 2.3 0 2.1 1.3 2.8 2.3 0
2.6 1.7 2.6 1.3 2.7 0 1.2 0
7.0 2.3 3.2 2.2 4.0 1.1 0 0
6.2 3.6 6.2 3.4 6.2 0 2.4 5.4
0 1.4 6.2 2.6 3.7 3.2 2.4 0
9.4 3.8 5.2 3.6 3.6 1.1 0 0
0 0.9 2.0 3.1 1.4 0 2.4 0
0 1.2 3.2 0.6 0.6 1.4 2.3 5.5
0 1.5 2.4 1.7 3.0 2.1 3.2 0
0 0 1.7 4.1 6.3 6.5 11.2 0
1.0 0.5 0 -0.5 -1.0
$\cos\theta$
2206C12

Fig. 12

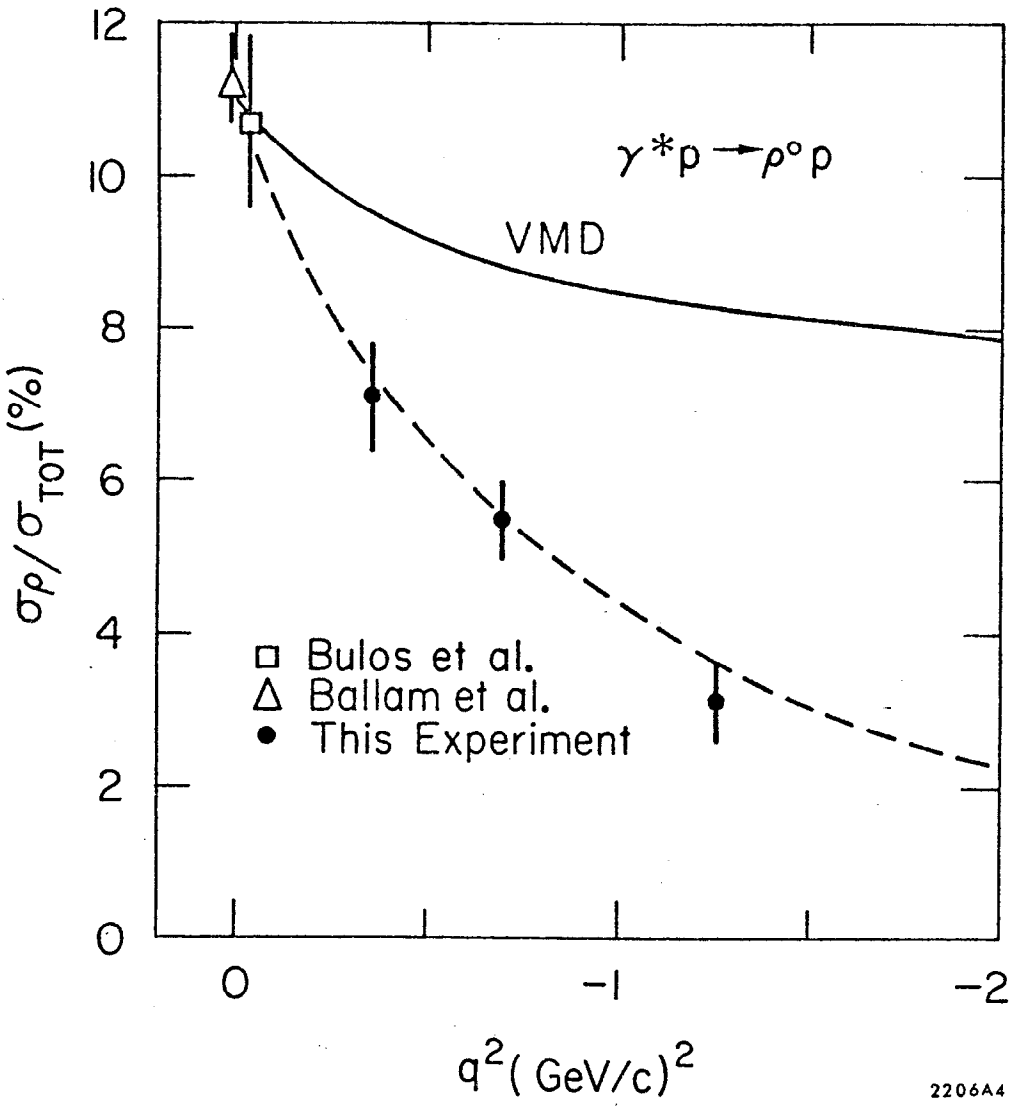
12
10
8
6
4
2
0
σ_ρ/σ_{TOT} (%)
$\gamma^* p \rightarrow \rho^\circ p$
VMD
Bulos et al.
Ballam et al.
This Experiment
0
-1
-2
q^2 (GeV/c)^2
2206A4

Fig. 13

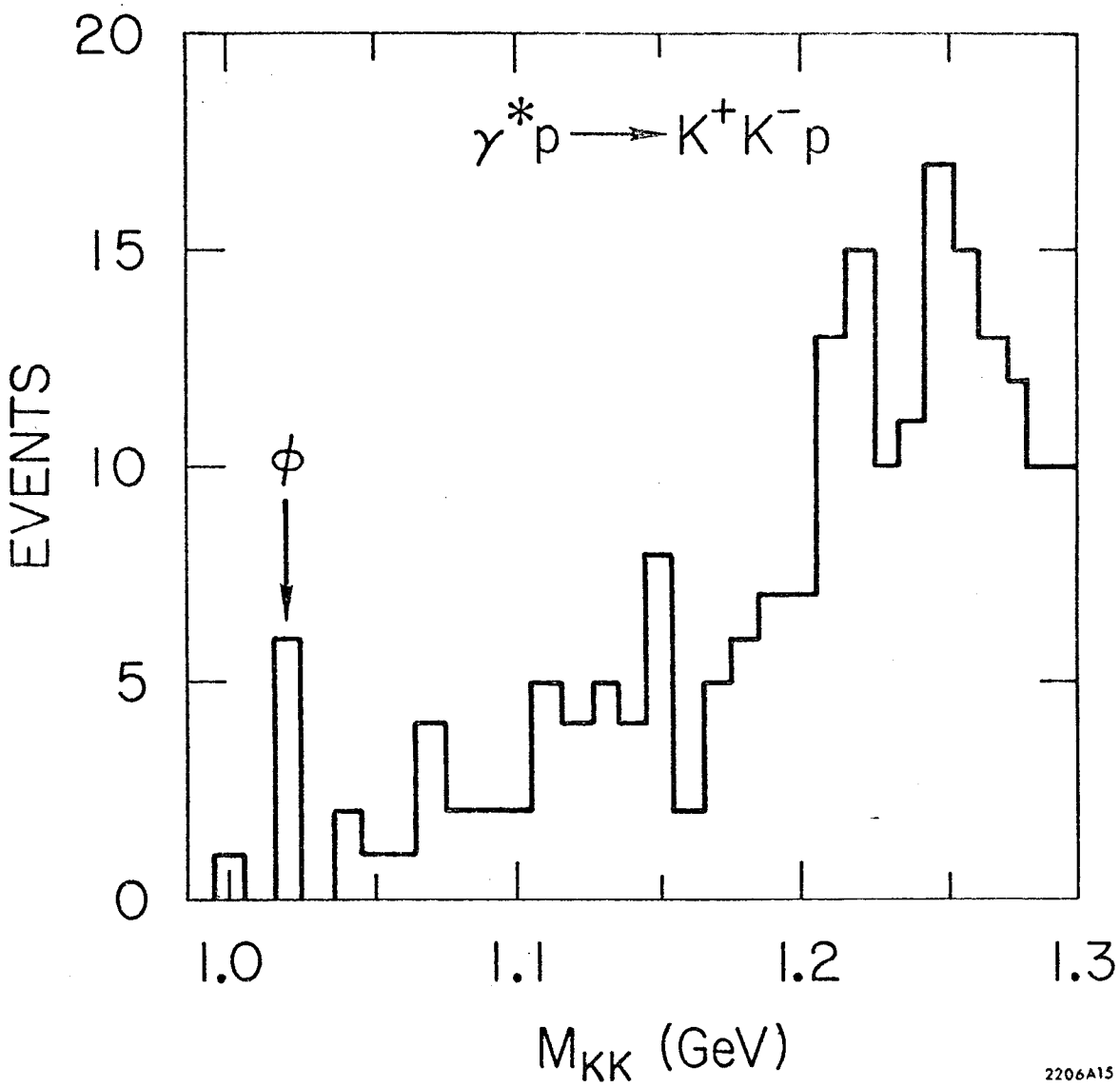
20
15
10
5
0
EVENTS
$\gamma^* p \longrightarrow K^+ K^- p$
ϕ
1.0
1.1
1.2
1.3
M_{KK} (GeV)
2206A15

Fig. 14

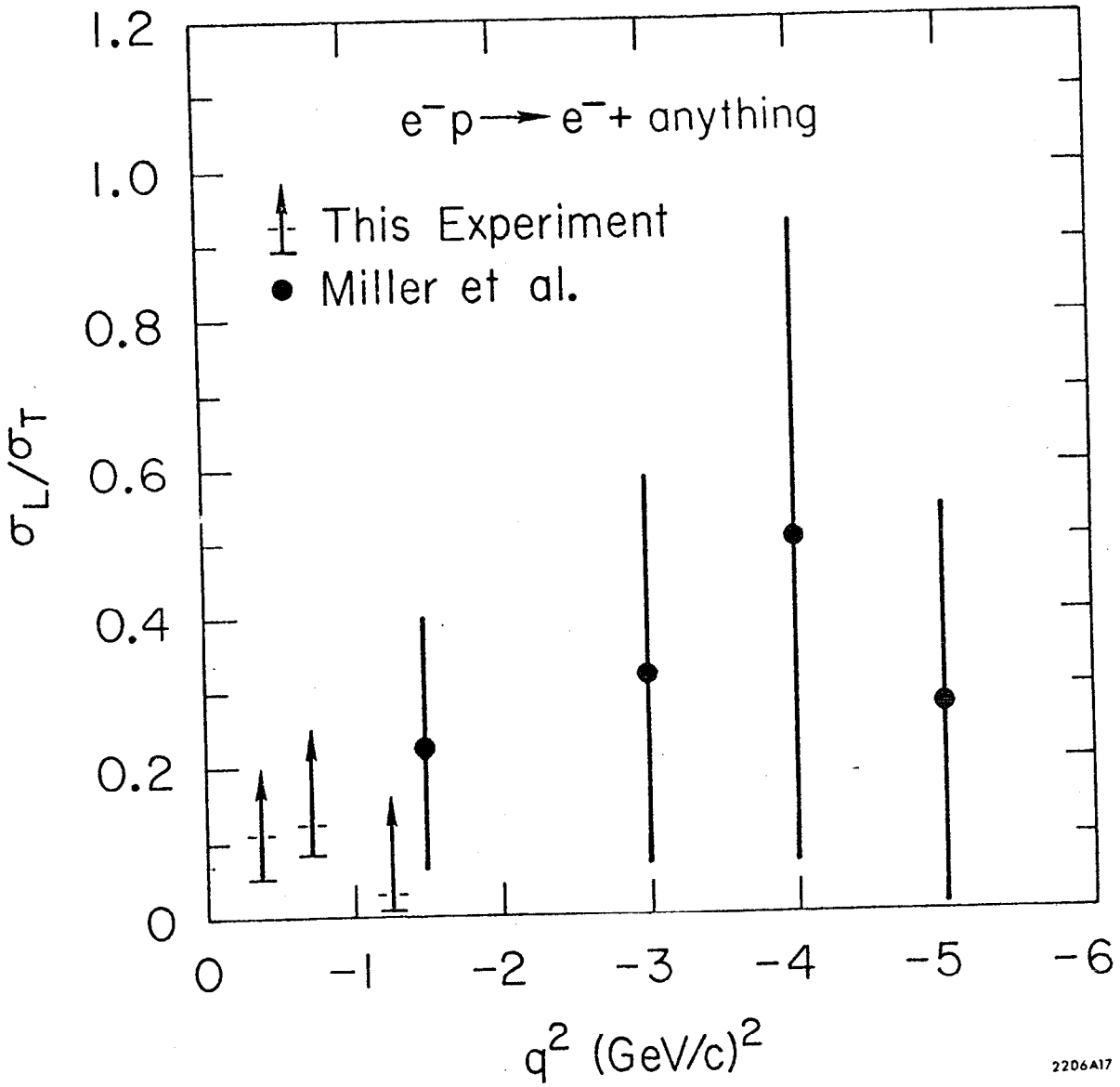
1.2
1.0
0.8
0.6
0.4
0.2
0
σ_L/σ_T
$e^-p \rightarrow e^- +$ anything
This Experiment
Miller et al.
0
-1
-2
-3
-4
-5
-6
q^2 (GeV/c)^2
2206A17

Fig. 15